Functional networks of inhibitory neurons orchestrate synchrony in the hippocampus

Marco Bocchio[1,2*], Artem Vorobyev[1*], Sadra Sadeh[3], Sophie Brustlein[1], Robin Dard[1], Susanne Reichinnek[1], Valentina Emiliani[3], Claudia Clopath[3] and Rosa Cossart[1]

1. Aix Marseille Univ, Inserm, INMED, Turing Center for Living Systems, Marseille, France
2. Department of Psychology, Durham University, Durham, UK
3. Wavefront-Engineering Microscopy Group, Photonics Department, Vision Institute, Sorbonne University , INSERM, CNRS, Paris, France.
4. Department of Brain Sciences, Imperial College London, London, UK
5. Department of Bioengineering, Imperial College London, London, UK.

Abstract

Inhibitory interneurons are a critical component of cortical circuits. Beyond providing inhibition, they have been proposed to coordinate the firing of excitatory neurons within cell assemblies. While many studies have dissected the function of specific interneuron subtypes, the relationship between interneurons and pyramidal cell synchrony *in vivo* remains unclear. We use an all-optical approach to simultaneously record hippocampal interneurons and pyramidal cells, and test the network influence of single interneurons. We show that CA1 interneurons form a functionally interconnected network that promotes synchrony through disinhibition during awake immobility without altering endogenous cell assemblies. A network model indicates that cell assemblies and dense but unspecific connectivity between interneurons are necessary ingredients to explain our experimental results. Thus, interneurons may not only operate via division of labor, but also through concerted activity. Our data challenge the idea of a purely decorrelating or segregating function of inhibition.

Introduction

Inhibitory interneurons expand the computational repertoire of cortical circuits, preventing runaway excitation[1], contributing to the generation of network oscillations[2] and regulating inputs and outputs of glutamatergic principal neurons[3]. Interneurons have been extensively studied for their morpho-functional diversity[4] and roles in behavior[5] . However, it remains unclear how interneurons regulate the dynamics of neuronal assemblies in cortical networks.

A critical role of inhibitory interneurons in stabilizing neuronal networks with recurrent excitatory connections has been demonstrated both in theoretical and experimental work[6]. Theoretical and *in vitro* work suggests that in such 'inhibition-stabilized networks' (ISNs), interneurons reduce pyramidal cells' firing rates and pairwise correlations[7,8], thus playing an inhibitory and desynchronizing role. However, this scenario is difficult to reconcile with the observation that in ISNs stimulating interneurons paradoxically increases the firing of excitatory cells[9]. Additionally, it remains unclear which role interneurons exert *in vivo*, particularly in neuronal networks where recurrent connections between excitatory neurons are sparse and recurrent connections are primarily mediated by interneurons.

The CA1 region of the adult hippocampus is an example of recurrent inhibitory network. In contrast to most cortical regions where recurrent connectivity mainly involves glutamatergic

excitatory synapses, the GABAergic inhibitory recurrent circuitry is the main support of CA1 local connectivity[10]. CA1 interneurons are highly interconnected and receive feedback inputs from a large number of diversely tuned pyramidal cells[11–19]. In addition, almost all (over 90%) of the local inputs onto a given CA1 pyramidal cell originate from interneurons[20]. As such, interneurons are ideally placed to sense and influence the activity of their local partners.

An organized functional network structure with defined assemblies underlies hippocampal function[21–23]. Accumulating evidence indicates that such functional organization arises intrinsically through mechanisms grounded in local circuits, with minimal reliance on external inputs[24,25]. This is particularly well established for the synchronous network events associated with sharp-wave ripples, which occur during quiet wakefulness or sleep, when external environmental influences are minimal[26]. In this mode, hippocampal assemblies are largely orthogonal, that is the activation of one inhibits the activation of others [27], indicating that interneurons could suppress competing assemblies.

A well-accepted view of the *in vivo* function of hippocampal interneurons posits that they control the formation and tuning of place cells[18,20,28,29]. According to this view, interneurons are simply feedback elements that ensure sparse spatial representations by inhibiting competing pyramidal cells, effectively segregating assemblies[30]. In addition, interneurons have been extensively studied for their class-specific tuning for defined behaviors and network oscillations[31–36]. However, these perspectives fail to explain how interneuron activity is coordinated at the population level, and how inhibition contributes to the shaping of cell assemblies.

Several lines of evidence suggest that inhibition could be directly involved in organizing pyramidal cells into assemblies. First, interneurons can synchronize multiple pyramidal cells[37]. Second, interneurons modulate various types of network oscillations that organize the firing of principal cells[38–41]. Third, slice experiments have shown that the stimulation of single inhibitory neurons can modulate population bursts in the developing and adult hippocampus[40,42]. Again, these observations appear largely at odds with a decorrelating role of inhibition[7,8].

To clarify the role of interneurons in population dynamics and synchrony, we have used an all-optical approach to study interneuron activity in relation to the CA1 network. We have combined two-photon calcium imaging in mice running spontaneously on a non-motorized treadmill[27,43,44] with holographic light stimulation [45] of single interneurons using a soma-targeted opsin[46]. We show that CA1 interneurons favor the co-activity of pyramidal cells in the form of pairwise correlations and Sharp Wave Ripples (SWRs)-associated network bursts, ultimately orchestrating pyramidal cell assemblies. Our data indicate that this paradoxical effect of inhibition is driven by disinhibitory mechanisms leading to protracted imbalance of excitation/inhibition (E/I). This amplification contrasts with feature-specific suppression of the visual cortex[47] and could reflect the different nature of the underlying recurrent connectivity. Hence, our results challenge current views of inhibitory interneurons, usually believed to trigger network decorrelations[7,8] and to be simple feedback elements segregating pyramidal cell assemblies[30,48].

Results

Imaging the activity of interneurons and pyramidal cells in CA1 in vivo

In order to describe the contribution of GABAergic interneurons to local hippocampal dynamics *in vivo*, we expressed the genetically-encoded calcium indicator GCaMP6m in both pyramidal cells and interneurons of the CA1 hippocampus (Fig. 1a, see Methods). To identify interneurons, we expressed the red protein tdTomato in GAD67-expressing neurons (Fig. 1a). A chronic glass window was implanted just above the dorsal hippocampus to image the

calcium dynamics of CA1 pyramidal cells and interneurons using two-photon microscopy. Mice were head-fixed and free to run in the dark on a non-motorized treadmill allowing spontaneous movement in conditions minimizing external sensory influences.

In these conditions, CA1 dynamics organize into sequences of neuronal firing during run and synchronous calcium events (SCEs) during rest periods[27,44]. These SCEs often co-occur with SWRs and activate functionally orthogonal cell assemblies, as previously shown[27]. We focused on the *stratum pyramidale* of the CA1 region where interneurons can be imaged together with excitatory principal cells. Each field of view (FOV) allowed for the simultaneous imaging of 254±104 pyramidal cells and 11±3 interneurons (means ± standard deviations; ranges: 115-402 and 8-15, respectively, n=11 FOVs from 6 mice). In line with the classical observation of interneurons displaying higher firing rates than pyramidal cells[49,50], we found that interneurons showed higher amplitude changes in their calcium fluorescence signal from baseline compared to pyramidal cells (p=0.007, Wilcoxon signed rank test, n=11 FOVs from 6 mice, Fig. 1c and Extended Data Fig. 1a). This suggests that, although calcium fluorescence signals are unlikely to report all the spikes fired by an individual neuron, our experiments captured an accurate read-out of pyramidal cell and interneuron physiology. Pyramidal cells and interneurons displayed similar behavioral state-dependent activity, with, on average, increased activity from rest to locomotion (pyramidal cells: p<0.001, interneurons: p=0.041, n=11 FOVs from 6 mice, Wilcoxon signed rank tests, Fig. 1d). In line with this, the excitation to inhibition ratio (E/I, see Methods) did not change between rest and locomotion (p=0.8, n=11 FOVs from 6 mice, Wilcoxon signed rank test, Fig. 1e). Next, we asked to what extent interneurons displayed conjoint activity. We found that pairwise Pearson's correlations between interneurons were higher than correlations between pyramidal cells (Fig. 1f-g, whole recording: p=0.003), and this difference was not behavioral state-dependent (rest periods: p=0.002; locomotion: p=0.01, all Wilcoxon signed rank tests, n=11 FOVs from 6 mice). This indicates that, although interneurons show higher morpho-physiological diversity than pyramidal cells, their activity is organized even more strongly in units of co-active neurons.

The activity of CA1 interneurons is linked to pyramidal cells co-activity

Next, we sought to understand whether interneurons orchestrate pyramidal cell co-activity. We found that the more a single pyramidal cell was correlated to interneurons (on average), the more it was also correlated to other excitatory neurons (pairwise Pearson's correlations; linear regression: $p=8e^{-25}$, $R^2=0.755$, n=2793 pyramidal cells, 11 FOVs, 6 mice, Fig.1h and Extended Data Fig. 1c), suggesting that interneuron activity could either just balance or even promote the synchronous recruitment of pyramidal cells. To extend this observation, we examined interneuron activity in relation to SCEs occurring during rest[27] (Fig. 1i). SCEs occurred at a frequency of 0.06±0.04 Hz (n=11 FOVs from 6 mice), a rate similar to previous observations and to the frequency of sharp-wave ripples in the awake state[27]. We observed that interneurons were present in the vast majority of SCEs, and that the proportional recruitment of pyramidal cells and interneurons in SCEs was similar (p=0.9, Wilcoxon signed-rank test, n=11 FOVs from 6 mice, Fig. 1i and Extended Data Fig. 1b). Additionally, Pearson's correlations of individual pyramidal cells with interneurons positively predicted the proportion of SCEs pyramidal cells participated to (linear regression: $p = 4e^{-49}$, $R^2 = 0.089$, n=2793 pyramidal cells, 11 FOVs, 6 mice, Fig. 1i). In line with this, pyramidal cells that were highly recruited in SCEs (scoring above the 90th percentile in the distribution of participation including all pyramidal cells from all recordings) showed significantly higher pairwise Pearson's correlations with interneurons compared to other pyramidal cells (≤90th percentile, $p=1.1e^{-24}$, Mann Whitney U test, highly active pyramidal cells: n=276; other pyramidal cells: n=2517, Fig. 1i).

We conclude that the CA1 region hosts a balanced network both at population and single-cell level, with interneurons being more functionally connected than their excitatory partners. In addition, the more a cell displayed coordinated firing with interneurons, the more likely it was to be recruited within SCEs. Altogether, rather than a decorrelating role, this suggests a contribution of interneurons to the coordination of activity in the CA1 region.

All-optical interrogation of CA1 interneurons in vivo

In order to go beyond these observations and probe causality, we next tested the network influence of single interneurons using holographic photostimulation of an excitatory opsin[51,52] combined with calcium imaging. With this aim, we expressed the fast soma-targeted opsin ST-ChroME in GAD67-expressing CA1 neurons (interneurons) and GCaMP6m in all neurons (interneurons and pyramidal cells, Fig. 2c). For simultaneous calcium imaging and photostimulation we used a custom-build set-up with two LASER sources (920 and 1030 nm) for both imaging and optogenetic activation (Fig. 2a1). Mice were head-fixed and imaged in the same conditions as above. They spontaneously alternated between run and rest periods (n=11 mice). After a baseline epoch of calcium imaging lasting 20 minutes, a single interneuron was targeted in the FOV for photoactivation by a train of light pulses every 30 seconds. The stimulation period lasted 5 minutes and was followed by a 5 minutes-long recovery period (i.e. no stimulation, Fig. 2a2). In this way, each targeted neuron was stimulated 10 times per stimulation period. A total of 149 interneurons from 53 FOVs were stimulated. We first quantified how efficient the stimulation was per targeted cell by computing the fraction of the stimulation trials that induced a significant calcium response (see Methods). When considering all the trials from all the neurons, we found that about a third of the trials induced a significant response (433 out of 1490 trials). This rate is comparable to previous reports[53]. However, the stimulation efficiency was not evenly distributed among targeted interneurons (Fig. 2a). Indeed, a few of them responded to less than 10% of the trials (21%, n=32 ‘low-response’ cells) while only a minority (15%) were reliably entrained by the stimulation and responded to more than 60% of the trials (n=22 ‘high-response’ cells). The remaining majority (64%) responded to between 10 and 60% of the trials (n=95 “medium-response” cells). Of note, cells displaying higher baseline activity exhibited a greater success rate (Pearson r=0.206, p=0.012, Extended data Fig. 2c). We also performed control experiments in mice for which interneurons expressed tdTomato instead of the opsin and found an average success rate of 8% of the trials (19 targeted cells, 7 mice). With these control experiments we can conclude that “low-response” (less than 10% of the trials) cells can be also defined as “unresponsive”.

Optical activation of single interneurons differentially modulates the activity of other interneurons and glutamatergic cells

We next asked whether the stimulation of a single interneuron could in turn induce a significant modulation of the activity of other imaged cells. To this end, we examined all the non-stimulated neurons and compared their calcium fluorescence between a window of one second prior to stimulation and a window of one second after stimulation. We used a Z-score-based method to identify significantly modulated cells (see Methods). We found that the activity of a small subset of imaged cells (62 neurons from 23 FOVs in 6 mice) could be identified as positively or negatively modulated by the stimulation of single interneurons (Fig. 3b-c). There was a significant correlation between the number of neurons displaying indirect positive or negative modulation (n=39 and n=23, respectively) and the fraction of successful stimulation trials in the target cell (Pearson's r=0.251, p=0.002, Pearson's r=0.295, p=0.0003,

respectively, Extended data Fig. 2d). No cells were indirectly modulated in the control experiments (19 trials, 7 mice). Single cell influence mapping experiments performed in the visual cortex indicated a pre-existing functional relationship between the stimulated neuron and the cells indirectly modulated by the stimulation [47]. In order to test whether this was the case for single interneuron stimulation in CA1, we computed the baseline Pearson's correlations between pairs of stimulated and indirectly modulated cells. Our results showed that both positively (n=39) and negatively (n=23) modulated cells tended to display a higher correlation with the stimulated neuron during baseline compared to unmodulated cells, but the difference was not statistically significant (Kruskal–Wallis H-test, three groups, p=0.17, see Extended Data Fig. 2b). The anatomical distance from the stimulated interneuron was not significantly different between modulated and unmodulated cells (Kruskal–Wallis H-test, three groups, p=0.08, Extended data Fig. 2a).

A further question was whether directly modulated neurons were glutamatergic or GABAergic. We found that positively modulated cells were evenly distributed among pyramidal cells and interneurons (0.13% and 0.11%, Z=-0.16, p=0.87), but interneurons tended to be more negatively modulated than pyramidal cells (0.07% and 0.64%, Z=1.87, p=0.06, Fig. 3c-d). Hence, we found a relatively similar proportion of positively- (68%) and negatively- (32%) modulated cells among the excitatory cell population (n=56 neurons) while an imbalance (Barnard's exact test: p = 0.038) was observed within the interneuron population, which displayed a majority of negatively modulated cells (83%, n=6 cells). This imbalance could lead to a possible disinhibitory network effect. Accordingly, we found a significant decrease by 17+-35%, (see Methods, n=734 interneurons, 11 mice) in global inhibition during the stimulation period as compared with the baseline (t-test p=0.0023).

Network modeling reveals that neuronal assemblies and unspecific inhibition are required for effects of single interneuron stimulation

To gain further insights into the circuit mechanisms underlying the functional integration of interneurons into local CA1 circuits, we simulated neuronal networks with global connectivity patterns similar to CA1. Our network model was composed of NE = 1000 excitatory (E) and NI = 100 inhibitory (I) neurons, with sparse connectivity between E neurons (EE: 1%). Connections between E and I neurons, and specifically within I neurons, were dense (EI: 50% and II: 85%), in keeping with our experimental results (high I-I correlations in Fig. 1g).

In addition, we implemented a variable subnetwork structure, whereby neurons belonging to the same subnetwork had stronger weights, forming cell assemblies. This was parameterized by a weight modulation factor (m), where m=1 corresponds to highly specific subnetworks and m=0 represents random connections without specificity (see Methods). Based on previous results on the presence of assemblies in CA1[27,54,55], we chose mEE=1 and mEI=1. We chose nonspecific connectivity for I-I connections (mII=0), based on our experimental results (Fig. 1g).

We then tested the effect of stimulating single interneurons in the model on the activity of other neurons (Fig. 3a). We assessed what fraction of E and I neurons decreased or increased their activity as a result of stimulating all interneurons (Fig 3a). Inhibitory neurons were mainly suppressed, while the effect on excitatory neurons was diverse. Some E neurons decreased their activity, but a larger fraction of E neurons in fact increased their activity, presumably as a result of effective disinhibition in the network. Overall, the result was similar to our experimental findings (cf. 2d and Fig. 3a).

The large-scale rate-based network models can be analyzed in terms of their responses in the steady state[56], giving us the possibility to predict the results from the weight matrix directly. We performed such an analysis and obtained the same results (Extended Data Fig. 3a), confirming that the effects described above arise from the connectivity structure. We then used this analytical insight to look into the main ingredients of the connectivity which led to the differential effects of single interneuron stimulation on E and I neurons. We found that both E-I subnetwork structure and denser and less specific I-I connectivity were important for these results. First, in network models with no subnetwork structure (mEE=0 and mEI=0, Fig. 3b), equal fractions of E neurons showed increase or decrease in their activity upon single interneuron stimulation (Fig. 3b), although I neurons were mainly suppressed (due to higher density of I-I connections). Second, when we allowed for a similar subnetwork structure for I-I connections with the same connection density (i.e., mII=1 and II=50%) as E-I connections, E and I neurons showed similar behavior, with slight dominance of positive changes (Fig. 3c). The differential behavior could be retrieved when we made the I-I connections denser but still specific (mII=1 and II=85%), although suppression of I neurons was not as dominant as before (Extended Data Fig. 3a). We therefore conclude that both subnetwork structure within E-I connections and denser coupling of I-I connections are crucial to explain the result of our single interneuron stimulations in CA1.

To mimic synchronous SCE-like activity in our model network and cross-check our model and empirical data, we stimulated excitatory neurons with external inputs (Fig. 3d). The external input was delivered in synchronous bouts to a fraction of excitatory neurons with functional proximity (i.e., close to each other in the subnetwork space) (see Methods for details), to emulate the input from CA3 to CA1. First, we observed average higher activity for I neurons, although E neurons were directly activated by the external stimulus (Fig. 3d). These results were consistent with our experimental observations (Fig. 1c). Higher activity of I neurons was a result of strong recurrent E-I connectivity in our network models, enabling a smaller number of I neurons to compensate for increases in the activity of more numerous E neurons.

Stimulating a fraction of E neurons led to a general suppression of activity in other E neurons (Fig. 3d), including those close to the stimulated neurons in assembly structure (i.e., in subnetwork space). This was a result of strong and specific E-I connectivity in the network structure, as reflected in the strong and specific recruitment of I neurons (Fig. 3d). These results argue for a general inhibition rather than competition between subnetworks. We also quantified pairwise correlations between E and I neurons and found correlations structures consistent with our experimental results (Fig. 1g). On average, the correlations were highest between I-I pairs, intermediate for E-I pairs, and lowest for E-E pairs, although there was a wide distribution of E-E correlations (Fig 3d). The general structure of correlations was preserved when we stimulated I neurons instead of E neurons, although in terms of activity, inhibitory neurons were suppressed in this case (Extended Data Fig. 3b). E neurons showed a general inhibition, with neurons functionally closer to inhibitory neurons receiving more suppression, and some surround E neurons being disinhibited (Extended Data Fig. 3b).

Interneuron activity is linked to pyramidal cell assemblies

Hence, in addition to the specific functional connectivity patterns of CA1, our simulations indicate that the presence of subnetwork structure in the form of mixed cell assemblies, comprising interneurons and pyramidal cells, is essential to explain our experimental observations. Thus, we next analyzed the contribution of interneurons to cell assemblies in our experimental dataset. First, we detected the cell assemblies nested in SCEs

using a k-means-based method[27]. We detected significant cell assemblies in 7/11 FOVs from 5 mice (2±2 assemblies per FOV, mean ± standard deviation, range: 1-6 assemblies, Fig. 4a). Consistent with a proportional representation of interneurons in SCEs, we found that the proportion of pyramidal cells and interneurons forming cell assemblies was similar ($p=0.51$, Wilcoxon signed-rank test, n=11 FOVs from 6 mice, Fig. 4a and Extended Data Fig. 5b). Additionally, we observed that pyramidal cells that were part of cell assemblies showed higher Pearson's correlations to interneurons compared to pyramidal cells not recruited into cell assemblies ($p=4e^{-11}$, Mann Whitney U test, pyramidal cells in assemblies: n=49; pyramidal cells not in assemblies: n=361, 11 FOVs, 6 mice). Thus, interneurons either function in balancing the coordinated activation of pyramidal cells into assemblies, or directly promote their recruitment into cell assemblies.

According to classical theories, hippocampal interneurons mainly operate in a feedback manner and segregate competing cell assemblies[30,48]. We wished to test whether our experiment revealed inhibition of competing pyramidal cells by interneurons. To this end, we examined the assembly activation-triggered average of pyramidal cells' calcium traces when each interneuron in an assembly was active or inactive (Fig. 4a). Activity of competing assemblies or of pyramidal cells not forming assemblies was similar regardless of whether the interneuron in an assembly was active or inactive (Fig. 4a4). On average, the calcium transients of the same assembly were reduced in amplitude when the interneuron was inactive, but this effect was not statistically significant ($p=0.7$, Wilcoxon signed-rank test, n=7 FOVs with significant assemblies from 5 mice). Thus, our data do not speak in favor of a segregating role of interneurons. Such empirical evidence is consistent with our model showing global inhibition rather than competition between subnetworks (Fig 3d).

To confirm that the observations on cell assemblies were not restricted to the detection method or were simply a reflection of the link between interneurons and SCEs, we employed a second cell assembly detection method not restricted to rest periods and SCEs. We used a procedure based on principal component analysis to detect significant assemblies, followed by independent component analysis to extract the weight of each neuron for each assembly[57] (see Methods for details). We detected significant assemblies in all 11 FOVs, with 3±2 assemblies per FOV (range: 1-6 assemblies). In keeping with a proportional contribution of pyramidal cells and interneurons to cell assemblies described previously, we observed similar assembly weights in pyramidal cells and interneurons ($p=0.4$, Wilcoxon signed rank test, n=31 assemblies from 11 FOVs from 6 mice, Extended Data Fig. 5c). In line with a positive relationship between interneurons and synchrony, we found that interneuron weights in a defined assembly predicted (positively) the weights of pyramidal cells ($p=2.3e^{-5}$, $R^2 = 0.862$, Extended Data Fig. 5c, n=11 FOVs, 31 assemblies, 6 mice). This indicates that higher interneuron participation is linked to stronger pyramidal cell co-activity. Thus, with both assembly methods, interneurons did not cluster into a single assembly but appeared intermingled across all cell assemblies. Consistent with this, the pairwise Pearson's correlations between interneurons were not significantly higher than the correlations between interneurons and pyramidal cells ($p=0.167$, Wilcoxon signed rank test, n=11 FOVs from 6 mice, Extended Data Fig. 5a). Furthermore, pyramidal cell assembly weights were more clustered in a single assembly compared to interneurons (maximum assembly weight across assemblies divided by the absolute average of assembly weights; $p = 0.0025$, Mann Whitney U test, n=31 assemblies, from 11 FOVs from 6 mice, Extended Data Fig. 5c). This indicates that interneurons contribute to assembly activity in a more unspecific fashion. We conclude that interneurons contribute to cell assemblies proportionally to their representation within local

circuits, potentially favoring their recruitment but, at least in our experimental conditions, not mediating cell assembly segregation.

Causal involvement of single interneurons in SCEs

Since single interneuron activation results in an unbalanced local modulation of excitatory and inhibitory cells that could lead to an increased network excitability, we asked whether this impacted population dynamics and in particular the synchronous network bursts occurring during rest in the form of SCEs. SCEs occurred at a frequency similar to the previous experiments (0.04±0.02 Hz, n=24 FOVs from 5 mice). In the experiments with "medium-response" and "high-response" cells (10% and more responses), we observed a significant decrease in the inter-SCE intervals (Mann-Whitney test, p=0.035) and increase in the SCE amplitude (number of co-activated cells) (Mann-Whitney test, p=0.0007) of SCEs during the stimulation period compared to baseline (18 FOVs, 5 mice, Extended Data Fig. 4a). Both of these changes were more prominent (Mann-Whitney test, p=0.01 and p=0.007, respectively) in the case of "highly-responsive" cells (more than 60% responses, Fig. 4b). In contrast, "unresponsive" cells did not induce any significant change in the amplitude or frequency of SCEs (Mann-Whitney test, p = 0.45 and p = 0.13, respectively). Importantly, this change in network dynamics did not reflect a change in behavior since run epochs were similarly distributed during baseline and stimulation periods (Z=-0.51, p=0.61). We conclude that the stimulation of single interneurons enhances network synchrony in CA1.

Single interneuron stimulation favors the reinstatement of endogenous assemblies

We last asked whether the network influence of single interneurons was modifying the endogenous functional structure of local circuits, including the organization of cell assemblies. To test whether the functional structure of our imaged network was affected by single interneuron stimulation, we first analyzed whether the cell assemblies composing SCEs (as defined in[27], see Methods) were affected. In total, we detected 96 assemblies during the baseline periods consisting of an average of 9 cells across 55 experimental sessions (out of total 141, from 6 mice). To determine the impact of stimulation on these assemblies, we first examined whether the stimulation evoked a significant time-locked response (activation or suppression) among cell assembly members. To this aim we computed the average of the calcium fluorescence traces of cell assembly members within a 10 seconds time window centered on the time of the stimulation and used a Z-score based test to determine whether the fluorescence signal just after the stimulation was significantly different from just before (see Methods). We found that about one third of the assemblies (29 out of 96) were significantly modulated by single-interneuron stimulation (Fig. 4c). The majority (58%) of the significantly modulated assemblies were activated following the stimulation (17 out of 29) while the rest were suppressed (12 out of 29). Therefore, single interneuron stimulation can lead to cell assembly activation or suppression.

Next, we examined the impact of interneuron stimulation on cell assembly composition. To this aim, we determined the cell assembly composition during the baseline, and compared it with the combined stimulation and post-stimulation periods (in order to have enough SCEs to perform cell assembly clustering). We calculated for each cell pair found in the same assembly during stimulation/post-stimulation periods, the fraction of them that already belonged to the same assembly during baseline (Fig. 4c2). We found a remarkable preservation of cell assembly membership since all of the pairs recruited in the same assembly during or just after stimulation were already part of a similar assembly during baseline (median 100%, n=236 pairs, 3 mice). We conclude that single interneuron stimulation can suppress or

activate cell assemblies, while preserving the endogenous population code, as predicted in our model.

Discussion

Using calcium imaging and holographic single-neuron photoactivation, we show that CA1 interneurons form a functionally connected network that promotes synchrony between pyramidal cells, especially in the form of SCEs occurring during awake immobility. Interneuron subcircuits operate within a balanced network where the activity of inhibitory cells matches that of excitatory ones across different behavioral states and at single neuron level. Optical activation of single interneurons triggers a transient disinhibition that favors network synchrony, but does not alter the endogenous functional organization of cell assemblies. In agreement with our computational simulations, we propose that the ability of single interneurons to promote synchrony in CA1 results from such rigid modular organization in cell assemblies and the preferential interconnectivity among interneurons, rather than the intrinsic features of specific interneuron subtypes.

Paradoxical synchrony-promoting effects of inhibitory interneurons in CA1

Our results challenge the intuitive idea that inhibitory interneurons mostly promote network desynchronization. We show that the more a single pyramidal cell correlates to interneuron activity, the more it correlates to other pyramidal cells and it is recruited in SCEs and cell assemblies. Additionally, optical stimulation of single interneurons increased both frequency and amplitude of SCEs, and modulated cell assembly activity (in the majority of cases enhancing recruitment of cell assemblies). In CA1, recurrent excitatory connectivity between pyramidal cells is low, and local interactions between pyramidal cells are primarily mediated by inhibitory interneurons[10]. Furthermore, approximately 20% of CA1 interneurons are interneuron-selective interneurons mediating disinhibition of pyramidal cells[58–60]. Tracing experiments calculating the relative contribution of interneurons versus local principal cells to the synaptic inputs onto CA1 interneurons[20] are needed to see whether an imbalance comparable to the one reported in the dentate gyrus[61] applies to CA1. In any case, we have shown that interneurons are typically inhibited by stimulation of a single CA1 interneuron, speaking in favor of a disinhibitory effect through the dense recurrent inhibitory network in CA1, as supported by our simulations. It remains unclear whether these synchrony-promoting effects are a general feature of cortical networks or if they are favored by the anatomical connectivity of the CA1 region of the hippocampus. Similar single cell optogenetic experiments have been performed in the upper layers visual cortex, where recurrent synapses are mostly glutamatergic[47]. In these conditions, the fine tuning of inhibition relies on specific functional links between excitatory and inhibitory cells.

The increase in SCEs frequency and amplitude triggered by interneuron stimulation may also be mediated by other mechanisms than connectivity. One example could be depolarizing GABA[62]. Although this may seem implausible in the adult brain *in vivo*, recent evidence suggests that the reversal potential for GABA is more depolarized during prolonged wakefulness [63]. One interesting alternative possibility that would combine both specific interneuron connectivity and intrinsic cell properties is the recently described persistent interruption of parvalbumin-expressing interneuron firing following brief inhibitory synaptic input[64]. Alternative options are plasticity of interneuron synapses, gap junction coupling between interneurons and long-range interactions with external structures such as the medial septum or the entorhinal cortex. The increase in SCE frequency caused by single interneuron activation is likely to be indirect because SCEs were not locked to the stimulation (although in

many cases cell assemblies were), and the proportion of positively modulated neurons was low. This could indicate that modulation of SCEs and cell assemblies may be caused by a slow buildup in the network, for instance mediated by a change in E/I. Future modeling work using biologically-detailed models will be instrumental in suggesting specific mechanisms supporting single interneuron-mediated synchronization.

Going beyond interneuron subtypes

Our findings expand the functional role of hippocampal interneurons *in vivo*. Thus far, many studies focused on pyramidal cell to interneuron functional connectivity, proposing that interneurons are feedback units recruited by pyramidal cell ensembles (place cells) to prevent runaway excitation or inhibit competing assemblies[16,17,30,48]. In contrast, our study puts a spotlight on interneurons to pyramidal cell directionality, demonstrating that interneurons are powerful controllers of network dynamics.

Our study examined the CA1 pyramidal layer because this allows simultaneous monitoring of large ensembles of pyramidal cells and interneurons. Since a large proportion of interneurons in this layer is formed by basket cells and axo-axonic cells[14], it is reasonable to assume that the effects we described are mediated, at least in part, by perisomatic targeting interneurons. This is consistent with large unitary inhibitory responses in the local field potential observed when stimulating single basket cells[65,66] and with theoretical work showing that parvalbumin-expressing basket cells strengthen and stabilize pyramidal cell assemblies[67]. Other inhibitory cells that could play a role are interneuron-selective interneurons (which is in line with the prevalent inhibition of interneurons observed) or dendrite-targeting ivy and bistratified cells. Importantly, results may be different when stimulating single interneurons in other layers, which are populated by different cell types. Still, variability in the ability of a single interneuron to exert a strong network influence appeared to correlate mostly with the reliability of light entrainment rather than anything else. Therefore, we would like to propose that single-interneuron influence is exerted by interneuron interconnectivity rather than specificity. This is somehow in agreement with a previous study putting forward an overall functional homogeneity of interneurons[20]. Future studies could clarify whether the variability in the effects of stimulation is influenced by cell type, or perhaps also by brain state. For instance, stimulating an interneuron during rest, when activity is typically reduced, may produce different or more detectable responses in the network. In addition, this study was performed in conditions where the mice are not running towards any specific goal and deprived of external sensory influences. In these conditions, hippocampal dynamics are dominated by self-referenced representations[44,68–70] and the influence of single interneurons in other contexts may be different.

We previously showed that hippocampal SCEs often occur during SWRs[27]. In line with the interneuron modulation of SCEs, interneuron-pyramidal cell interactions have been shown to be crucial for SWRs[71,72]. In particular, stimulation of perisomatic interneurons of the pyramidal layer both suppresses, and subsequently enhances, the generation of SWRs[40]. This demonstrates that hippocampal network dynamics occurring during rest (SWRs/SCEs) are, to a large extent, internally generated.

Implications and limitations

The behavioral implications of interneuron-mediated enhancement of synchrony remain to be established. Given the importance of SWRs for memory consolidation [55,73,74], one possibility is that CA1 interneurons of the pyramidal layer coordinate memory consolidation during rest by promoting network bursts. In line with this hypothesis, inhibition of parvalbumin-

expressing interneurons in CA1 after learning impairs fear memory consolidation and pyramidal cell firing coherence[75].

This study reveals that the E/I ratio remains balanced across brain states, with CA1 interneurons recruited in SCEs and cell assemblies in similar proportions to pyramidal cells. However, analysis of the distribution of individual cells' weights across assemblies showed that interneurons are less associated to a single assembly than pyramidal cells. This is consistent with what we previously observed for early-born inhibitory hub cells[43]. Our data indicate that interneurons tend to promote assembly activation, rather than only assembly segregation. We found no evidence of spontaneous assembly segregation by single interneurons. Optical activation of single interneurons caused assembly activation in approximately 60% of the cases, and inhibition in 40%. We also found that activating single interneurons triggered activation of previously active assemblies, rather than creating new associations between neurons. This observation provides further support to the concept that hippocampal dynamics are preconfigured by functional connectivity[76,77].

There are important limitations to consider when interpreting our results. First, calcium imaging has a low temporal resolution compared to electrophysiology. This implies that short-delay fast dynamics may be missed by our analyses (for instance transient inhibitions followed by excitation). Additionally, it is unclear how much calcium dynamics are able to disclose inhibitory responses. Thus, we cannot fully exclude that assembly segregation mediated by inhibition plays a stronger role when recording from CA1 neurons with high temporal resolution. However, we did find that the majority of indirectly modulated interneurons displayed inhibitory responses. Finally, calcium imaging is unlikely to reveal all the spikes fired by CA1 neurons. The amount of spikes revealed by calcium-related fluorescence is particularly uncertain when examining fast spiking populations. To the best of our knowledge, no study to date performed dual electrophysiology and calcium imaging recordings from interneuron populations to provide a convincing benchmark. Thus, we cannot exclude that heterogeneities in interneuron recruitment observed with calcium imaging may be due to inherent differences in the spike-to-calcium relationship for the different subtypes. Nonetheless, we found that interneurons, on average, display significantly higher ΔF/Fs than pyramidal cells, indicating that calcium imaging is able to detect their higher firing rates.

Conclusion

We provide converging experimental and modeling evidence for a role of single interneurons in triggering synchrony and endogenous cell assembly activation, rather than merely balancing excitation. This is likely due to the close interconnectivity between interneurons in adult CA1. In developing cortical circuits, single interneurons appear to control synchrony in the opposite direction (Bollmann et al. in press). Thus, the present finding has broad and important implications, including in pathology, such as epilepsy, where spatial coding deficits are related to disrupted interneuron synchronization [78].

Acknowledgements

We thank all the members of the Cossart lab for helpful discussions and constructive feedback. We thank INMED's animal facility and PBMC technological platform for excellent technical support. This work was supported by the European Research Council under the European Union's Horizon 2020 research and innovation program (grant agreement no. 646925 and 951330), by the Fondation Bettencourt Schueller, the Fondation Roger de Spoelberch, and by the French National Research Agency (grant agreement no ANR-14-CE13-0016); A. V. was supported by the ITN Marie Curie (H2020-MSCA-ITN-2017, project

765549). R.C. is supported by CNRS. S. S was funded by the Wellcome Trust (225412/Z/22/Z). V.E acknowledges the Fondation Bettencourt Schueller (Prix Coups d'Elan pour la Recherche Française) and the ERC Advanced Grant HOLOVIS (ERC-2019-AdG; award no. 885090). M.B. was supported by the European Union (Marie Skłodowska-Curie individual fellowship, grant No. 794861—IF-2017).

Authors' contributions

A.V., M.B, and R.C. designed experiments; A.V, M.B, S.B. and S.R. performed experiments; A.V., and M.B analyzed the data; R.D. provided some analysis scripts. S.S. and C.C. performed the modeling work. A.V, M.B, S.S, C.C. and R.C. wrote the paper. V.E. designed the optical system for holographic stimulations. R.C. conceived and supervised the project.

Methods

Animals

All experimental procedures were approved by the French ethics committee (Ministère de l'Enseignement Supérieur, de la Recherche et de l'Innovation (MESRI); Comité d'éthique CEEA-014; APAFiS #28.506) and were conducted in agreement with the European Council Directive 86/609/EEC.

GAD67-Cre mice were kindly donated by Dr. Hannah Monyer (Heidelberg University). Ai14 reporter mice were purchased from Jackson Laboratories (B6;129S6-Gt(ROSA)26Sor$^{tm14(CAG-tdTomato)Hze/J}$, strain # 007908). Mice were bred and stored in an animal facility with room temperature (RT) and relative humidity maintained at 22 ± 1°C and 50 ± 20%, respectively. Mice were provided *ad libitum* access to water and food.

GCaMP6m, tdTomato and ST-ChroME expression

GCaMP6m expression was obtained by injection of a viral vector in the dorsal CA1 in adult mice or in the lateral ventricle in newborn pups at P0. tdTomato expression in GABAergic neurons was achieved by crossing GAD-Cre mice with Ai14 reporter mice or by injecting a floxed viral vector expressing tdTomato either in the dorsal CA1 in adult mice or in the lateral ventricle in newborn pups at P0.

For viral injections in the CA1 of adult mice, GAD67-Cre mice (8-12 weeks of age) were anesthetized using 1–3% isoflurane in oxygen. Analgesia was also provided with buprenorphine (Buprecare, 0.1 mg/kg). Lidocaine cream was applied before the incision for additional analgesia. Mice were fixed to a stereotaxic frame with a digital display console (Kopf, Model 940). Under aseptic conditions, an incision was made in the scalp, the skull was exposed, and a small craniotomy was drilled over the target brain region. A recombinant viral vector was delivered using a glass pipette pulled from borosilicate glass (3.5" 3-000-203-G/X, Drummond Scientific) and connected to a Nanoject III system (Drummond Scientific). The tip of the pipette was broken to achieve an opening with an internal diameter of 25–35 µm. To express GCaMP6m, was injected AAV1.Syn-GCaMP6m (pAAV.Syn.GCaMP6m.WPRE.SV40 from Addgene, #100841, titer 6-8 $\times$ 10^{12}). To express tdTomato in GABAergic neurons, AAV9-FLEX-tdTomato was injected (pAAV-FLEX-tdTomato from Addgene, #28306, titer 3 $\times$ 10^{12}). Viruses were diluted in D-phosphate-buffered saline (PBS), Sigma Aldrich). To target the dorsal CA1, we injected 600 nL at a rate of 25 nL/min at the coordinates below. All coordinates are in millimeters. Anteroposterior (AP) coordinates are relative to bregma; mediolateral (ML) coordinates are relative to the sagittal suture; dorsoventral (DV) coordinates are measured from the brain surface. Dorsal CA1: −2 AP, −2 ML (300 nL at −1.3 DV and 300 nL at -1.25 DV).

For P0 injections, we followed previously published procedures [79,80]. Briefly, mouse pups were anesthetized by hypothermia. GAD67-Cre mouse pups were injected in the left hemisphere. To reach the ventricle, we injected in a position that was roughly two fifths of an imaginary line drawn between lambda and the left eye at a depth of 0.4 mm. Correct injection was verified by the spread of the blue dye. To express ST-ChroME in GABAergic neurons, AAV9.DIO-ST-ChroME-P2A-H2B-mRuby3 was used (pAAV-CAG-DIO-ChroME-ST-P2A-H2B-mRuby3 from Addgene, #108912, titer 2.7 $\times$ 10^{12}).

In vivo 2-photon calcium imaging

A chronic cranial window was implanted using previously published procedures[27,43,44]. Mice were head-fixed on a non-motorized treadmill allowing self-paced locomotion (adapted from

[29]) All experiments were performed in the dark. No reward was given. After three to five habituation sessions, mice were alert but calm and alternated between periods of locomotion and rest during imaging. The treadmill was made of a 180 cm black velvet seamless belt lacking tactile or visual cues mounted on two wheels. The movement of the treadmill was monitored using two pairs of LEDs and photo-sensors that read patterns from a disk attached to one of the wheels. For all experiments, extra sound, odor, touch, and light were minimized during the imaging session. Imaging was performed with a single beam multiphoton laser scanning system coupled to a microscope (TriM Scope II, Lavision Biotech). The Ti: sapphire excitation laser (Chameleon Ultra II, Coherent) was operated at 920 nm for GCaMP6m excitation and at 1030 nm for tdTomato excitation. Fluorescence emission was acquired using a 16× objective (Nikon, NA 0.8) and split in two detectors (GaSP PMT, H7422-40, Hamamatsu) with bandpass filters of 510/10 nm for GCaMP6m and 580/20 nm for tdTomato. Scanner and PMTs were controlled by a commercial software (Imspector, Lavision Biotech). To optimize the signal-to-noise ratio of fluorescence variation, we used a dwell time exposition of 1.85 µs and a spatial resolution of 2 µm/pixel that allowed us to acquire at 8-10 Hz at a field of view of 400 × 400 µm. Locomotion and imaging triggers were synchronously acquired and digitized using a 1440A Digidata (Axon instrument, 2 kHz sampling) and the pClamp 10 software (Molecular Devices).

In vivo 2-photon calcium imaging with simultaneous holographic optogenetic stimulation

As in the experiments without holographic optogenetic stimulation, a chronic cranial window was implanted using previously published procedures [27,43,44]. Mice were head-fixed on a non-motorized treadmill allowing self-paced locomotion (adapted from [29]). All experiments were performed in the dark with no reward. After a brief habituation period, mice began to alternate between periods of locomotion and rest during imaging. The movement of the animal was recorded using Phenosys SpeedBelt treadmill. The optical system was a custom-built microscope combining galvo-based two-photon scanning with Computer Generated Holography[45,81,82]. Raster scanning of calcium fluorescence signals was achieved using standard galvo scanners and a pulsed femtosecond imaging LASER source. The LASER beam (Chameleon Ultra II, Coherent) was expanded with two lenses telescope assembly (f = 300 mm, f = 500 mm) and projected onto an XY galvo mirror pair (6215H, Cambridge Technology) controlled with two servo driver cards (67125H-1HP-FS60, Cambridge Technology). A half-wave plate (#AWHP10M-980, Thorlabs) and a polarizer (#GT10-B, Thorlabs) were used to adjust LASER power. Next, a scan and a tube lens (focal length fS = 50 mm and fT = 375 mm, respectively) were used to conjugate the XY scanner focal plane to the back focal plane of the microscope objective (16x Nikon, N.A 0.8). This configuration allowed scanning a field of view of 280 µm * 280 µm (256 pixels * 256 pixels) at the focal plane of the objective with a framerate of 8.4Hz and a power of 50mW at 920 nm wavelength. To collect the emitted fluorescent signal, the back focal plane of the objective and the focal plane of a GaAsP PMT (Hamamatsu, H7244-20) were conjugated through a relay of lenses (f = 100 mm, #AC254-100-A, Thorlabs, f = 25 mm, #LA1951-A, Thorlabs). Two spectral filters were mounted in front of the PMT (FF01-770/SP-25, Semrock, ET520/40m, Chroma) to optimize GFP detection. The analog signal was next converted from current to voltage and amplified through a transimpedance amplifier (#TIA60, Thorlabs). Finally, an electronic card (NI6356, National Instruments) in combination with Scanimage software (Vidriotechnologies) was used to control the scanners and to digitalize the analog signal from the PMT.

Photostimulation of neurons of interest used Computer Generated Holography. Briefly, the beam of the pulsed femtosecond photoactivation LASER (GOJI, AMPLITUDE SYSTEMS,

10MHz repetition rate, 1030nm) was shaped by a Spatial Light Modulator (Hamamatsu, LCOS-SLM X13138-07). The size of the LASER beam was expanded using a two-lense telescope assembly (#AC254-030-B, Thorlabs, #AC254-150-B, Thorlabs) so that it covered the entire surface of the SLM. A half-wave plate (#AHWP10M-980, Thorlabs) was used to align the polarization of the laser to the orientation of the liquid crystals. Three lenses (#AC508-300-B) combined with the tube lens (fT = 375 mm) in a 4-f configuration enabled conjugating of the SLM focal plane to the back focal plane of the microscope objective. The zero-order of the SLM was suppressed with a cylindrical lens (f = 300 mm, f = #LJ1558L1-B, Thorlabs) as described previously[83]. A custom software (Wavefront Designer IV) based on the Gerchberg & Saxton algorithm, was used to convert the photostimulation intensity pattern at the focal plane into a photostimulation phase mask addressed to the SLM[51].

To combine the two imaging and photostimulation paths, a dichroic mirror (#DMPSP1000L, Thorlabs) was placed at the focal plane of the scan lens. The custom software mentioned above was used to adjust the spatial overlap of the photostimulation pattern with the imaging at 920 nm thanks to a rhodamine fluorescent sample that was bleached at 1030 nm and imaged at 920 nm. To synchronize the paths, a Matlab script defined a photostimulation temporal gate and sent a TTL signal, *via* the NI card described above, to an obturator (Vincent shutter instruments) placed in front of the photostimulation LASER source during the raster scanning for calcium imaging. Holographic stimulation of targeted cells was achieved with an excitation spot of ~15 μm lateral size, corresponding to an axial resolution of 20μm. Trains of 5 consecutive pulses (75 ms period, 25% duty cycle, at 0.3-0.8 mW/μm2 power) were applied every 30 seconds during the stimulation period.

Each experimental session consisted of 20 minutes of baseline recording, followed by 5 minutes of selected cell stimulation and 5 minutes of post-stimulation recording. If the FOV contained more than one cell expressing both GCaMP6m and ChroME, the next cell was targeted and stimulated for 5 minutes, followed by 5 minutes of post-stimulation recording. On average, 3 cells per FOV were stimulated. The proportion of time spent running was not significantly different between successive stimulations (Kruskal-Wallis H-test, p=0.89).

Analysis of calcium imaging data

In vivo calcium movies were pre-processed using the Suite2p toolbox for Python [84]. Movies were motion-corrected using rigid and non-rigid registrations with a block size of approximately one fourth of the size of the FOV in pixels. Automatic cell detection was performed based on activity (tau: 1 ms, equivalent to the GCaMP6m time constant; cell diameter: 5-7 pixels). To ensure correct segmentation of somatic calcium activity, the automatic detection was manually refined by adding and removing regions of interest (ROIs) with visual inspection of mean, maximum projections and correlation images, as well as fluorescence traces. Subsequent analyses were performed using custom-made MATLAB (Mathworks, R2022b) and Python scripts. Locomotion epochs were defined as time periods with deflections in the photo-sensors signal reading the treadmill movement. Rest epochs were defined as periods >200 ms without treadmill movement.

ΔF/F was calculated using the formula:

$$\Delta F/F(i) = \frac{x(i) - F0(i)}{F0(i)},$$

where $F0(i)$ is the median value within a 60 seconds sliding window before the frame *i*. The E/I ratio was defined as the ratio between the average ΔF/F of pyramidal cells and average ΔF/F of interneurons.

Synchronous Calcium Events (SCEs) were detected using a previously published method[27]. A third-order Savitzky-Golay filter with a frame size of 500 ms was first applied on the fluorescence calcium signal of each cell. The threshold for detecting calcium transients was adapted for each time point and each cell as follows: it was the sum of the median value with three times the interquartile range calculated within a -2/+2 s sliding window. To avoid detecting twice the same calcium transient, the minimal delay between events was set to one second. Activity occurring during run epochs was not included in this analysis. SCEs corresponded to the synchronous calcium events that involved more cells than expected by chance within a 200 ms time window (i.e. >3 standard deviations after temporal reshuffling of cell activity) and with a minimum cell number equivalent to 5% of the cells in the FOV.

We used two different cell assemblies detection methods. The first one was based on SCEs and k-means clustering. The second on principal component analysis (PCA) and independent component analysis (ICA). For the first method, cell assemblies were identified using a clustering algorithm based on SCE similarity for cell participation followed by a statistical test for cell participation in each SCE cluster. The SCE similarity metric was the squared Euclidean distance between columns of the normalized covariance matrix. This similarity metric allowed a more efficient clustering. Unsupervised clustering of SCE was obtained by running the k-means algorithm on this metric with cluster numbers ranging from 2 to 19. Hundred iterations of k-means were run for each cluster number and the iteration that resulted in the best average silhouette value was kept. For a given element i, the silhouette value was computed using the following formula:

$$s = \frac{b - a}{max\{a,b\}}$$

where a is the average dissimilarity of i with all other elements in its cluster and b the lowest average dissimilarity of i to any other cluster. In this analysis, the dissimilarity metric was the normalized covariance. A random distribution of average silhouette values for each cluster was calculated by reshuffling cell participation across different SCE and applying the same algorithm. Clusters with average silhouette values exceeding the 95th percentile of the random case were considered as statistically significant. Each cluster of SCE was then associated with a cell assembly which comprised those cells that significantly participated in the SCE events within that particular cluster. Cell participation to a given cluster was considered statistically significant if the fraction of SCE in that cluster that activated the cell exceeded the 95th percentile of reshuffled data. If a cell was significantly active in more than one SCE cluster, it was associated with the one in which it participated the most (percentage wise).

The second method is a PCA/ICA algorithm extensively used to detect hippocampal cell assemblies in electrophysiological data[57]. Fluorescence traces were convolved with a Gaussian kernel and then Z-scored (to reduce the influence of baseline fluorescence). The number of significant co-activation patterns (assemblies) was estimated as the number of principal component variances above a threshold derived from the circularly shifted matrix including the fluorescence traces of all neurons. Assembly patterns (vectors including assembly weights of all individual neurons) were then extracted with ICA.

Data processing for stimulation experiments

In order to determine whether a stimulation (i.e. a 5 pulse train) evoked a significant calcium response on the target neuron, a dependent t-test was used to compare the values of the cell's raw fluorescence calcium signal 10 frames before (i.e. 1.2 seconds) and 10 frames after the stimulation. The stimulation was considered successful if the values after the stimulation were significantly ($p<0.05$) higher than before stimulation.

A z-score test was used to determine whether cells were indirectly modulated by the stimulation of a target neuron (activated or suppressed). For each stimulation, the fluorescence signal within a time window of 20 frames (i.e. 2.4 s) centered on the time of stimulation was considered. The median value for each time point within this interval was calculated. For the resulting trace, we calculated the z-score, using the formula

$$Z = \frac{x - \bar{x}}{\sigma}$$

both mean x̄ and standard deviation σ were calculated using the values before the stimulation. Modulated cells were selected using the following criteria: if the Z-score exceeded a value of 1.96 (95% criteria) for two consecutive time points, a cell was defined as positively modulated; if it dropped below -1.65 (90% criteria) for two consecutive time points, it was defined as negatively modulated. We chose different Z-score thresholds for positively and negatively modulated cells to account for calcium imaging's difficulty in detecting activity suppression (see [85]).

Assembly modulation was analyzed using the same z-score-based test as above but using the mean fluorescence of all the cells in the assembly.

Changes in global inhibition were estimated using the ΔF/F of the calcium fluorescence traces of interneurons. To calculate the percentage of change, we found the median difference between the ΔF/F values of the baseline period and the stimulation period. We also performed a dependent t-test on the data from the same periods to determine the significance of this change.

Network modeling of neuronal responses

We simulate the activity of a network of N neurons composed of N_E excitatory and N_I inhibitory units ($N = N_E + N_I$). The dynamics of neuronal activity is simulated by solving the following differential equations:

$$\tau\, dr_E(t)/dt = -r_E(t) + \Phi[W_{EE} r_E(t) + W_{EI} r_I(t) + s_E(t)] \quad [1]$$
$$\tau\, dr_I(t)/dt = -r_I(t) + \Phi[W_{IE} r_E(t) + W_{II} r_I(t) + s_I(t)]$$

which describe changes in the average firing rate of neurons as a function of external and recurrent inputs to them. Here, $r_E(t)$ and $r_I(t)$ are vectors of firing rates, composed of the activity of excitatory (E) and inhibitory (I) subpopulations at each time point, t. τ is the time constant of the network integration, and $\Phi(.)$ denotes the activation function, which is assumed to be a linear rectified function, namely: $\Phi(x) = 0$, if $x < 0$; $\Phi(x) = x$, if $x > 0$.

$s_E(t)$ and $s_E(t)$ denote the vectors of external inputs to E and I neurons, respectively, at each time point. All neurons receive a background input, which is modulated upon external perturbations or stimulation (this is described in detail in the section “External perturbation and stimulation”). The background input (s_b) consists of a mean component (μ_b) and a noise term (ζ): $s_b = \mu_b + \zeta$, where the noise term is drawn from a uniform distribution between $[0, \zeta_{max}]$ at each time step of simulation (dt). The equations are numerically solved by the forward Euler method.

Recurrent interactions between neurons are described by the weight matrix, W, with specific submatrices W_{YX} describing the connection weights from a presynaptic subpopulation X (E or I) to the postsynaptic subpopulation Y (E or I). We describe how these weight matrices are obtained in the following section.

Unless stated otherwise, default parameters are chosen as: $N_E = 1000$, $N_I = 100$, $\tau = 10$, $dt = 1$, $\mu_b = 1$, $\zeta_{max} = 4$.

Connections between pairs of neurons from a presynaptic population X to a postsynaptic population Y are established based on the density of connectivity (ϵ_{YX}). The connections are drawn from a binomial distribution with probability ϵ_{YX}, returning a connectivity matrix C_{YX} with 0 (no connection) or 1 (connected) entries. Self-connections are not permitted. Connections are assumed to be very sparse for E-E connections; for instance, $\epsilon_{EE} = 0.01$ means that an E

neuron is connected to 1% of other E neurons, on average. Other connection types are more densely established; for instance, $\epsilon_{IE} = 0.5$ means that, on average, 50% presynaptic E neurons are connected to a postsynaptic I neuron.

The strength of the established connections are determined by the parameter J. For a given submatrix, W_{YX}, J_{YX} denotes the average strength of connections. Each entry, w_{ij}(specifying the weight of connection from the j-th presynaptic neuron to the i-th postsynaptic neuron), is obtained as:

$$w_{ij} = J_{YX}\, c_{ij} \qquad [2]$$

where c_{ij} is the corresponding entry in the connectivity matrix denoting the presence (1) or absence (0) of a connection.

For nonspecific weight matrices ($m = 0$), J_{YX} is the same for all pairs of neurons (belonging to the presynaptic subpopulation X and postsynaptic population Y). The presence of subnetwork structure in CA1 is quantified by various degrees of specificity in different submatrices, with $m_{YX} = 1$ denoting the maximum specificity of connections weights from $X \to Y$, and $m_{YX} = 0$ recovering nonspecific weights. In either case, parameter m quantifies the modulation of weights between a pair of neurons according to their proximity in a functional space. This is emulated by arranging E and I neurons are on a ring, with parameter θ (ranging from $[0, \pi)$) specifying their location. The weight of a given pair of neurons is then obtained as:

$$w_{ij} = J_{YX}(1 + m_{YX}\ cos\ [2(\theta_i - \theta_j)])\ c_{ij} \qquad [3]$$

where θ_i and θ_j refer to the location of the i-th and the j-th neurons, respectively. E neurons are arranged to cover the range $[0, \pi)$ uniformly, such that the location of the k-th neuron is given by $\theta_k = \pi\ (k-1)/N_E$. Similarly, I neurons are arranged to cover the range uniformly, in an ordered manner corresponding to their IDs.

Closeby neurons on the ring will have smaller $\Delta\theta = \theta_i - \theta_j$, which translates to stronger weights than random, with neurons far away from each other by $\Delta\theta = \pi/4$ remaining at the nonspecific levels, and even farther pairs reducing their weights compared to random, with neurons with $\Delta\theta = \pi/2$ distance having the most negative modulation. Modulation of connection weights by parameter m, therefore, emulates the subnetwork structure in a continuous manner. Note that $m_{YX} = 0$ recovers the nonspecific weight condition described in Eq. 2.

Unless stated otherwise, the parameters are chosen as: $\epsilon_{EE} = 0.01$, $\epsilon_{IE} = \epsilon_{EI} = 0.5$, $\epsilon_{II} = 0.85$, $J_{EE} = J_{IE} = 0.002$, $J_{EI} = J_{II} = -0.02$, $m_{EE} = m_{EI} = m_{IE} = 1$, $m_{II} = 0$.

To simulate the effect of single interneuron perturbations in our model, we perturb inhibitory neurons individually and measure its impact on the rest of neurons. The external input to individual I neuron is increased, from its baseline level, by δs.

The activity of the network (Eq. 1) is simulated for T_{sim}, with and without this individual perturbation. The average activity of non-perturbed neurons are calculated, after discarding transient responses (T_{trans}). The change in the average activity of each neuron between the two condition is obtained, δr, and the influence is quantified as the normalized changes of activity following perturbations: $\delta r/\delta s$. This procedure is repeated for all N_I inhibitory neurons, and the distributions of influences are obtained for non-perturbed E and I neurons. The fraction of neurons in each subpopulation showing positive ($\delta r > 0$) or negative ($\delta r < 0$) changes are then quantified (as shown in Fig. M and Fig. Suppl).

Unless stated otherwise, default parameters are: $\delta s = 1$, $T_{sim} = 150$, $T_{trans} = 50$.

To measure the effect of external stimulation on our model networks, we stimulated a fraction (20%) of E or I neurons, which were chosen to be proximal on the ring (belonging to similar subnetworks). Stimulations were delivered as synchronous increases of the input to the selected neurons by δs within a total stimulation time of T_{stim}. Stimulus was turned on for ΔT_{ON} (the input to stimulated neurons were increased to $s_b + \delta s$) and turned off for ΔT_{OFF} (the input to all neurons went back to the baseline level, s_b) in between. The average changes in the activity of other, nonstimulated neurons were obtained by calculating the mean response during stimulation, after discarding the transient responses (the initial T_{trans}). This was compared to the average responses, which were obtained from independent simulations

without stimulation. The difference of the responses was obtained as changes in the activity following stimulation for each neuron (as shown in Fig. M-F and Fig. Suppl-C). We also calculated the pairwise correlation of activity between all pairs of neurons during the stimulation (which is shown in Fig. M-G and Fig. Suppl-D).
The parameters are chosen as: $\delta s = 1$, $T_{stim} = 1000$, $\Delta T_{ON} = 50$, $\Delta T_{OFF} = 150$, $T_{trans} = 50$, $\epsilon_{EE} = 0.01$, $\epsilon_{IE} = \epsilon_{EI} = 0.5$, $\epsilon_{II} = 0.85$, $m_{EE} = m_{EI} = m_{IE} = 1$, $m_{II} = 0$, $J_{EE} = J_{IE} = 0.002$, $J_{EI} = J_{II} = -0.01$.
The responses of the rate-based network model (Eq. 1) in the stationary state can be analyzed by letting $dr_E/dt = 0$ and $dr_I/dt = 0$, leading to:

$$r_E = \Phi[W_{EE}r_E + W_{EI}r_I + s_E] \quad [4]$$
$$r_I = \Phi[W_{IE}r_E + W_{II}r_I + s_I]$$

Changes in the stationary state responses upon external perturbations $(s + \delta s)$ can be obtained from linearized dynamics of the network about the equilibrium point:

$$\delta r = (I - W)^{-1}\delta s \quad [5]$$

where δs is the vector of all input changes, δr is the vector of all response changes, and W is the total weight matrix of the network, describing all the connections between E and I neurons. The effect of single inhibitory neuron perturbations can be evaluated from Eq. 5, when δs consists of 0s for all entries except for the perturbed neuron. We numerically solve Eq. 5 for each inhibitory neuron perturbation, and repeat the procedure for all inhibitory neurons to obtain similar measures of response changes as rate-based simulations. Our results from this linear analysis were in good match with the results obtained from the perturbations of rate-based dynamics (Fig. Suppl-A), suggesting our findings can be understood in terms of the structure of weight matrices.

Statistics
Statistical tests were performed in Python or MATLAB (R2022b). Pairwise comparisons between distributions were performed using the Mann–Whitney U test for unpaired groups and with the Wilcoxon signed rank test for paired groups. For pairwise correlations between neurons' activities, we used Pearson's correlations. To compare the proportion of positively and negatively modulated cells, we used the Barnard's test.

References

1. Trevelyan, A. J. & Schevon, C. A. How inhibition influences seizure propagation. *Neuropharmacology* **69**, 45–54 (2013).
2. Mann, E. O. & Paulsen, O. Role of GABAergic inhibition in hippocampal network oscillations. *Trends Neurosci.* **30**, 343–349 (2007).
3. Klausberger, T. & Somogyi, P. Neuronal diversity and temporal dynamics: the unity of hippocampal circuit operations. *Science* **321**, 53–57 (2008).
4. DeFelipe, J. *et al.* New insights into the classification and nomenclature of cortical GABAergic interneurons. *Nat. Rev. Neurosci.* **14**, 202–216 (2013).
5. Hangya, B., Pi, H.-J., Kvitsiani, D., Ranade, S. P. & Kepecs, A. From circuit motifs to computations: mapping the behavioral repertoire of cortical interneurons. *Curr. Opin.*

Neurobiol. **26**, 117–124 (2014).

6. Sadeh, S. & Clopath, C. Inhibitory stabilization and cortical computation. *Nat. Rev. Neurosci.* **22**, 21–37 (2021).
7. Renart, A. *et al.* The Asynchronous State in Cortical Circuits. *Science* **327**, 587–590 (2010).
8. Sippy, T. & Yuste, R. Decorrelating action of inhibition in neocortical networks. *J. Neurosci. Off. J. Soc. Neurosci.* **33**, 9813–9830 (2013).
9. Tsodyks, M. V., Skaggs, W. E., Sejnowski, T. J. & McNaughton, B. L. Paradoxical Effects of External Modulation of Inhibitory Interneurons. *J. Neurosci.* **17**, 4382–4388 (1997).
10. Takács, V. T., Klausberger, T., Somogyi, P., Freund, T. F. & Gulyás, A. I. Extrinsic and local glutamatergic inputs of the rat hippocampal CA1 area differentially innervate pyramidal cells and interneurons. *Hippocampus* **22**, 1379–1391 (2012).
11. Gulyás, A. I., Hájos, N., Katona, I. & Freund, T. F. Interneurons are the local targets of hippocampal inhibitory cells which project to the medial septum. *Eur. J. Neurosci.* **17**, 1861–1872 (2003).
12. Freund, T. f. & Buzsáki, G. Interneurons of the hippocampus. *Hippocampus* **6**, 347–470 (1996).
13. Lee, S.-H. *et al.* Parvalbumin-positive basket cells differentiate among hippocampal pyramidal cells. *Neuron* **82**, 1129–1144 (2014).
14. Bezaire, M. J. & Soltesz, I. Quantitative assessment of CA1 local circuits: knowledge base for interneuron-pyramidal cell connectivity. *Hippocampus* **23**, 751–785 (2013).
15. Ali, A. B., Deuchars, J., Pawelzik, H. & Thomson, A. M. CA1 pyramidal to basket and bistratified cell EPSPs: dual intracellular recordings in rat hippocampal slices. *J. Physiol.* **507 (Pt 1)**, 201–217 (1998).
16. Dupret, D., O'Neill, J. & Csicsvari, J. Dynamic reconfiguration of hippocampal interneuron circuits during spatial learning. *Neuron* **78**, 166–180 (2013).
17. English, D. F. *et al.* Pyramidal Cell-Interneuron Circuit Architecture and Dynamics in

Hippocampal Networks. *Neuron* **96**, 505-520.e7 (2017).

18. Rolotti, S. V. *et al.* Local feedback inhibition tightly controls rapid formation of hippocampal place fields. *Neuron* **110**, 783-794.e6 (2022).
19. Ego-Stengel, V. & Wilson, M. A. Spatial selectivity and theta phase precession in CA1 interneurons. *Hippocampus* **17**, 161–174 (2007).
20. Geiller, T. *et al.* Local circuit amplification of spatial selectivity in the hippocampus. *Nature* **601**, 105–109 (2022).
21. Drieu, C. & Zugaro, M. Hippocampal Sequences During Exploration: Mechanisms and Functions. *Front. Cell. Neurosci.* **13**, 232 (2019).
22. Cossart, R. & Khazipov, R. How development sculpts hippocampal circuits and function. *Physiol. Rev.* **102**, 343–378 (2022).
23. Buzsáki, G. & Tingley, D. Space and Time: The Hippocampus as a Sequence Generator. *Trends Cogn. Sci.* **22**, 853–869 (2018).
24. Braun, W. & Memmesheimer, R.-M. High-frequency oscillations and sequence generation in two-population models of hippocampal region CA1. *PLoS Comput. Biol.* **18**, e1009891 (2022).
25. Zutshi, I., Valero, M., Fernández-Ruiz, A. & Buzsáki, G. Extrinsic control and intrinsic computation in the hippocampal CA1 circuit. *Neuron* **110**, 658-673.e5 (2022).
26. Buzsáki, G. Hippocampal sharp wave-ripple: A cognitive biomarker for episodic memory and planning. *Hippocampus* **25**, 1073–1188 (2015).
27. Malvache, A., Reichinnek, S., Villette, V., Haimerl, C. & Cossart, R. Awake hippocampal reactivations project onto orthogonal neuronal assemblies. *Science* **353**, 1280–1283 (2016).
28. Grienberger, C., Milstein, A. D., Bittner, K. C., Romani, S. & Magee, J. C. Inhibitory suppression of heterogeneously tuned excitation enhances spatial coding in CA1 place cells. *Nat. Neurosci.* **20**, 417–426 (2017).
29. Royer, S. *et al.* Control of timing, rate and bursts of hippocampal place cells by dendritic and somatic inhibition. *Nat. Neurosci.* **15**, 769–775 (2012).

30. Geisler, C., Robbe, D., Zugaro, M., Sirota, A. & Buzsáki, G. Hippocampal place cell assemblies are speed-controlled oscillators. *Proc. Natl. Acad. Sci.* **104**, 8149–8154 (2007).
31. Dudok, B. *et al.* Recruitment and inhibitory action of hippocampal axo-axonic cells during behavior. *Neuron* **109**, 3838-3850.e8 (2021).
32. Geiller, T. *et al.* Large-Scale 3D Two-Photon Imaging of Molecularly Identified CA1 Interneuron Dynamics in Behaving Mice. *Neuron* **108**, 968-983.e9 (2020).
33. Katona, L. *et al.* Sleep and Movement Differentiates Actions of Two Types of Somatostatin-Expressing GABAergic Interneuron in Rat Hippocampus. *Neuron* **91**, 1183 (2016).
34. Lapray, D. *et al.* Behavior-dependent specialization of identified hippocampal interneurons. *Nat. Neurosci.* **15**, 1265–1271 (2012).
35. Turi, G. F. *et al.* Vasoactive Intestinal Polypeptide-Expressing Interneurons in the Hippocampus Support Goal-Oriented Spatial Learning. *Neuron* **101**, 1150-1165.e8 (2019).
36. Viney, T. J. *et al.* Network state-dependent inhibition of identified hippocampal CA3 axo-axonic cells in vivo. *Nat. Neurosci.* **16**, 1802–1811 (2013).
37. Cobb, S. R., Buhl, E. H., Halasy, K., Paulsen, O. & Somogyi, P. Synchronization of neuronal activity in hippocampus by individual GABAergic interneurons. *Nature* **378**, 75–78 (1995).
38. Amilhon, B. *et al.* Parvalbumin Interneurons of Hippocampus Tune Population Activity at Theta Frequency. *Neuron* **86**, 1277–1289 (2015).
39. Antonoudiou, P., Tan, Y. L., Kontou, G., Upton, A. L. & Mann, E. O. Parvalbumin and Somatostatin Interneurons Contribute to the Generation of Hippocampal Gamma Oscillations. *J. Neurosci.* **40**, 7668–7687 (2020).
40. Ellender, T. J., Nissen, W., Colgin, L. L., Mann, E. O. & Paulsen, O. Priming of Hippocampal Population Bursts by Individual Perisomatic-Targeting Interneurons. *J. Neurosci.* **30**, 5979–5991 (2010).

41. Evangelista, R. *et al.* Generation of Sharp Wave-Ripple Events by Disinhibition. *J. Neurosci.* **40**, 7811–7836 (2020).
42. Bonifazi, P. *et al.* GABAergic hub neurons orchestrate synchrony in developing hippocampal networks. *Science* **326**, 1419–1424 (2009).
43. Bocchio, M. *et al.* Hippocampal hub neurons maintain distinct connectivity throughout their lifetime. *Nat. Commun.* **11**, 4559 (2020).
44. Villette, V., Malvache, A., Tressard, T., Dupuy, N. & Cossart, R. Internally Recurring Hippocampal Sequences as a Population Template of Spatiotemporal Information. *Neuron* **88**, 357–366 (2015).
45. Chen, I.-W. *et al.* In Vivo Submillisecond Two-Photon Optogenetics with Temporally Focused Patterned Light. *J. Neurosci.* **39**, 3484–3497 (2019).
46. Mardinly, A. R. *et al.* Precise multimodal optical control of neural ensemble activity. *Nat. Neurosci.* **21**, 881–893 (2018).
47. Chettih, S. N. & Harvey, C. D. Single-neuron perturbations reveal feature-specific competition in V1. *Nature* **567**, 334–340 (2019).
48. Buzsáki, G. Neural syntax: cell assemblies, synapsembles, and readers. *Neuron* **68**, 362–385 (2010).
49. Csicsvari, J., Hirase, H., Czurkó, A., Mamiya, A. & Buzsáki, G. Fast network oscillations in the hippocampal CA1 region of the behaving rat. *J. Neurosci. Off. J. Soc. Neurosci.* **19**, RC20 (1999).
50. Ylinen, A. *et al.* Sharp wave-associated high-frequency oscillation (200 Hz) in the intact hippocampus: network and intracellular mechanisms. *J. Neurosci. Off. J. Soc. Neurosci.* **15**, 30–46 (1995).
51. Lutz, C. *et al.* Holographic photolysis of caged neurotransmitters. *Nat. Methods* **5**, 821–827 (2008).
52. Papagiakoumou, E., de Sars, V., Oron, D. & Emiliani, V. Patterned two-photon illumination by spatiotemporal shaping of ultrashort pulses. *Opt. Express* **16**, 22039–22047 (2008).

53. Sridharan, S. *et al.* High-performance microbial opsins for spatially and temporally precise perturbations of large neuronal networks. *Neuron* **110**, 1139-1155.e6 (2022).
54. Harris, K. D., Csicsvari, J., Hirase, H., Dragoi, G. & Buzsáki, G. Organization of cell assemblies in the hippocampus. *Nature* **424**, 552–556 (2003).
55. van de Ven, G. M., Trouche, S., McNamara, C. G., Allen, K. & Dupret, D. Hippocampal Offline Reactivation Consolidates Recently Formed Cell Assembly Patterns during Sharp Wave-Ripples. *Neuron* **92**, 968–974 (2016).
56. Sadeh, S. & Clopath, C. Theory of neuronal perturbome in cortical networks. *Proc. Natl. Acad. Sci.* **117**, 26966–26976 (2020).
57. Lopes-dos-Santos, V., Ribeiro, S. & Tort, A. B. L. Detecting cell assemblies in large neuronal populations. *J. Neurosci. Methods* **220**, 149–166 (2013).
58. Chamberland, S., Salesse, C., Topolnik, D. & Topolnik, L. Synapse-Specific Inhibitory Control of Hippocampal Feedback Inhibitory Circuit. *Front. Cell. Neurosci.* **4**, 130 (2010).
59. Pelkey, K. A. *et al.* Hippocampal GABAergic Inhibitory Interneurons. *Physiol. Rev.* **97**, 1619–1747 (2017).
60. Tyan, L. *et al.* Dendritic inhibition provided by interneuron-specific cells controls the firing rate and timing of the hippocampal feedback inhibitory circuitry. *J. Neurosci. Off. J. Soc. Neurosci.* **34**, 4534–4547 (2014).
61. Espinoza, C., Guzman, S. J., Zhang, X. & Jonas, P. Parvalbumin+ interneurons obey unique connectivity rules and establish a powerful lateral-inhibition microcircuit in dentate gyrus. *Nat. Commun.* **9**, 4605 (2018).
62. Kilb, W. When Are Depolarizing GABAergic Responses Excitatory? *Front. Mol. Neurosci.* **14**, (2021).
63. Alfonsa, H. *et al.* Intracellular chloride regulation mediates local sleep pressure in the cortex. *Nat. Neurosci.* **26**, 64–78 (2023).
64. Chamberland, S. *et al.* Brief synaptic inhibition persistently interrupts firing of fast-spiking interneurons. *Neuron* **111**, 1264-1281.e5 (2023).
65. Bazelot, M., Dinocourt, C., Cohen, I. & Miles, R. Unitary inhibitory field potentials in the

CA3 region of rat hippocampus. *J. Physiol.* **588**, 2077–2090 (2010).

66. Glickfeld, L. L., Roberts, J. D., Somogyi, P. & Scanziani, M. Interneurons hyperpolarize pyramidal cells along their entire somatodendritic axis. *Nat. Neurosci.* **12**, 21–23 (2009).
67. Cornford, J. H. *et al.* Dendritic NMDA receptors in parvalbumin neurons enable strong and stable neuronal assemblies. *eLife* **8**, e49872 (2019).
68. Sharif, F., Tayebi, B., Buzsáki, G., Royer, S. & Fernandez-Ruiz, A. Subcircuits of Deep and Superficial CA1 Place Cells Support Efficient Spatial Coding across Heterogeneous Environments. *Neuron* **109**, 363-376.e6 (2021).
69. Fattahi, M., Sharif, F., Geiller, T. & Royer, S. Differential Representation of Landmark and Self-Motion Information along the CA1 Radial Axis: Self-Motion Generated Place Fields Shift toward Landmarks during Septal Inactivation. *J. Neurosci.* **38**, 6766–6778 (2018).
70. Geiller, T., Fattahi, M., Choi, J.-S. & Royer, S. Place cells are more strongly tied to landmarks in deep than in superficial CA1. *Nat. Commun.* **8**, 14531 (2017).
71. Gan, J., Weng, S., Pernía-Andrade, A. J., Csicsvari, J. & Jonas, P. Phase-Locked Inhibition, but Not Excitation, Underlies Hippocampal Ripple Oscillations in Awake Mice In Vivo. *Neuron* **93**, 308–314 (2017).
72. Stark, E. *et al.* Pyramidal Cell-Interneuron Interactions Underlie Hippocampal Ripple Oscillations. *Neuron* **83**, 467–480 (2014).
73. Girardeau, G. & Zugaro, M. Hippocampal ripples and memory consolidation. *Curr. Opin. Neurobiol.* **21**, 452–459 (2011).
74. Maingret, N., Girardeau, G., Todorova, R., Goutierre, M. & Zugaro, M. Hippocampo-cortical coupling mediates memory consolidation during sleep. *Nat. Neurosci.* **19**, 959–964 (2016).
75. Ognjanovski, N. *et al.* Parvalbumin-expressing interneurons coordinate hippocampal network dynamics required for memory consolidation. *Nat. Commun.* **8**, 15039 (2017).
76. Dragoi, G. & Tonegawa, S. Preplay of future place cell sequences by hippocampal cellular assemblies. *Nature* **469**, 397–401 (2011).

77. McKenzie, S. *et al.* Preexisting hippocampal network dynamics constrain optogenetically induced place fields. *Neuron* **109**, 1040-1054.e7 (2021).

78. Shuman, T. *et al.* Breakdown of spatial coding and interneuron synchronization in epileptic mice. *Nat. Neurosci.* **23**, 229–238 (2020).

79. Dard, R. F. *et al.* The rapid developmental rise of somatic inhibition disengages hippocampal dynamics from self-motion. *eLife* **11**, e78116 (2022).

80. Kim, J.-Y., Grunke, S. D., Levites, Y., Golde, T. E. & Jankowsky, J. L. Intracerebroventricular Viral Injection of the Neonatal Mouse Brain for Persistent and Widespread Neuronal Transduction. *J. Vis. Exp. JoVE* 51863 (2014) doi:10.3791/51863.

81. Chaigneau, E. *et al.* Two-Photon Holographic Stimulation of ReaChR. *Front. Cell. Neurosci.* **10**, (2016).

82. Ronzitti, E. *et al.* Submillisecond Optogenetic Control of Neuronal Firing with Two-Photon Holographic Photoactivation of Chronos. *J. Neurosci. Off. J. Soc. Neurosci.* **37**, 10679–10689 (2017).

83. Hernandez, O. *et al.* Three-dimensional spatiotemporal focusing of holographic patterns. *Nat. Commun.* **7**, 11928 (2016).

84. Pachitariu, M. *et al.* Suite2p: beyond 10,000 neurons with standard two-photon microscopy. 061507 Preprint at https://doi.org/10.1101/061507 (2017).

85. Vanwalleghem, G., Constantin, L. & Scott, E. K. Calcium Imaging and the Curse of Negativity. *Front. Neural Circuits* **14**, (2021).

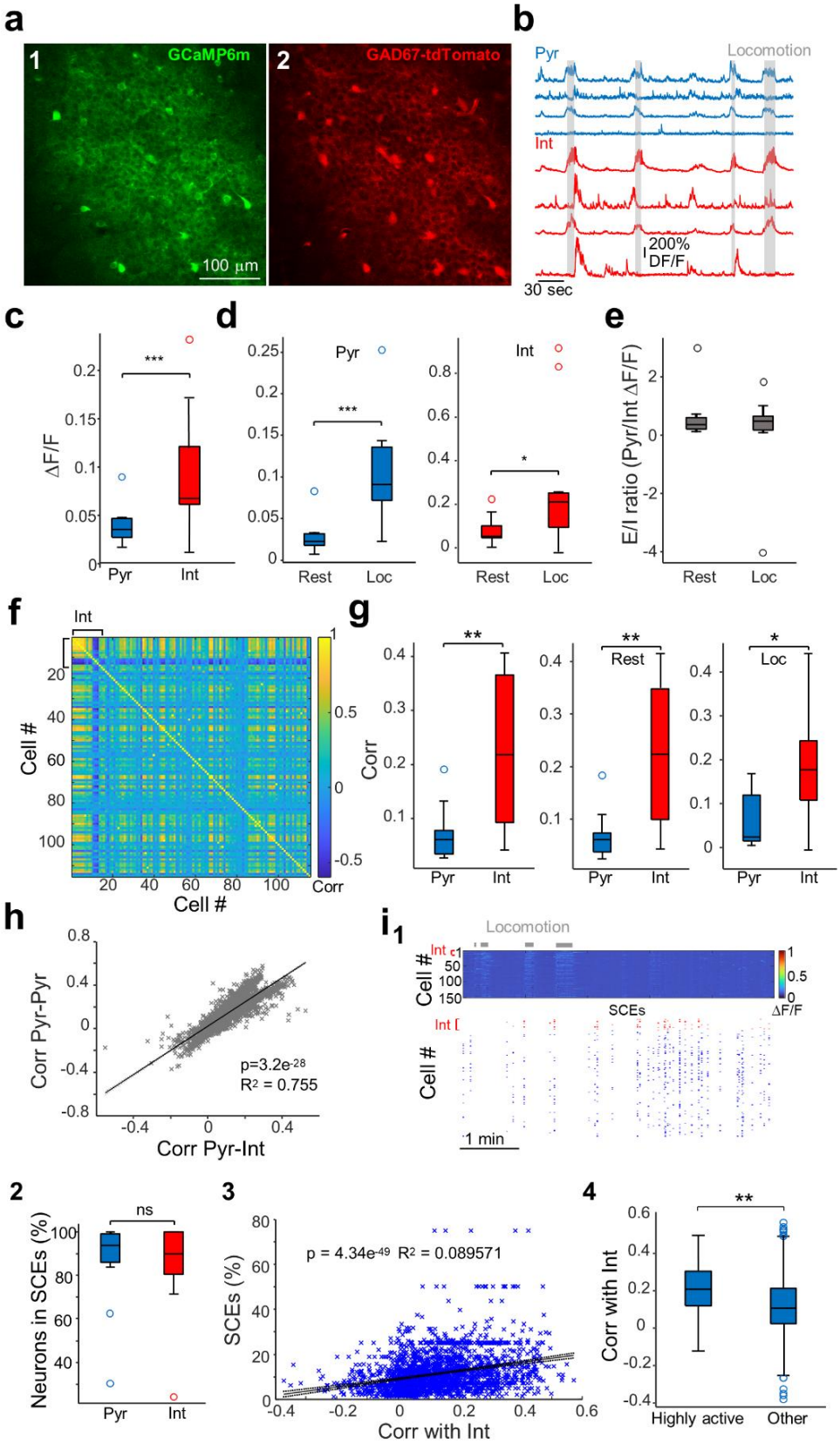

Figure 1 - CA1 interneuron activity is linked to pyramidal cell synchrony.

a. GCaMP6m and tdTomato signals to - respectively - record neural activity and identify interneurons. TdTomato is expressed under the control of the GABAergic promoter *GAD67*.

b. Example calcium ΔF/F traces from four pyramidal neurons (GAD67-negative) and four interneurons (GAD67-positive). Note the increased activity in most cells during locomotion and larger calcium transients in interneurons. **c.** Interneurons show higher calcium activity than pyramidal cells (p=0.007, Wilcoxon signed rank test, n=11 FOVs from 6 mice). **d.** Pyramidal cells (bluet) and interneurons (red) display increased activity during locomotion (pyramidal cells: p<0.001, interneurons: p=0.041, n=11 FOVs from 6 mice, Wilcoxon signed rank tests). **e.** E/I ratio (ratio between pyramidal cells and interneuron ΔF/F) remains stable across rest and locomotion (p=0.8, n=11 FOVs from 6 mice, Wilcoxon signed rank test). **f.** Correlation matrix for recording shown in a (including all 15 interneurons and 100 pyramidal cells). **g.** Pairwise Pearson's correlations between interneurons are higher than correlations between pyramidal cells. Left, whole recording: p=0.003. Middle: rest periods: p=0.002. Right: locomotion: p=0.01. All Wilcoxon signed rank tests, n=11 FOVs from 6 mice. **h.** Fit of linear model between pairwise Pearson's correlations of each pyramidal cell to interneurons and other pyramidal cells (n=2793 pyramidal cells, 11 FOVs, 6 mice). **i1.** Example of synchronous calcium events (SCEs) occurring during rest. Locomotion periods are marked in gray. *Top*, Heatmap shows the ΔF/F traces of all imaged neurons. Note the increased activity during locomotion. Interneuron traces are highlighted in red. *Bottom*, the raster plot shows the activity of imaged neurons during SCEs (see Methods for details on the detection method). Interneurons are highlighted in red, and pyramidal cells in blue. **i2.** Pyramidal cells and interneurons are recruited in SCEs in similar proportions (p=0.9, Wilcoxon signed-rank test, n=11 recordings from 6 mice). **i3.** Fit of linear model between Pearson's correlations of each pyramidal cell to interneurons and percentage of SCEs that cell participates to (n=2793 pyramidal cells, 11 recordings, 6 mice). **i4.** Pyramidal cells that are highly active in SCEs (scoring above the 90th percentile in the distribution of SCE participation including all pyramidal cells) display higher Pearson's correlations to interneurons compared to other pyramidal cells (<90th percentile, $p=1.1e^{-24}$, Mann Whitney U test, highly active pyramidal cells: n=276; other pyramidal cells: n=2517).

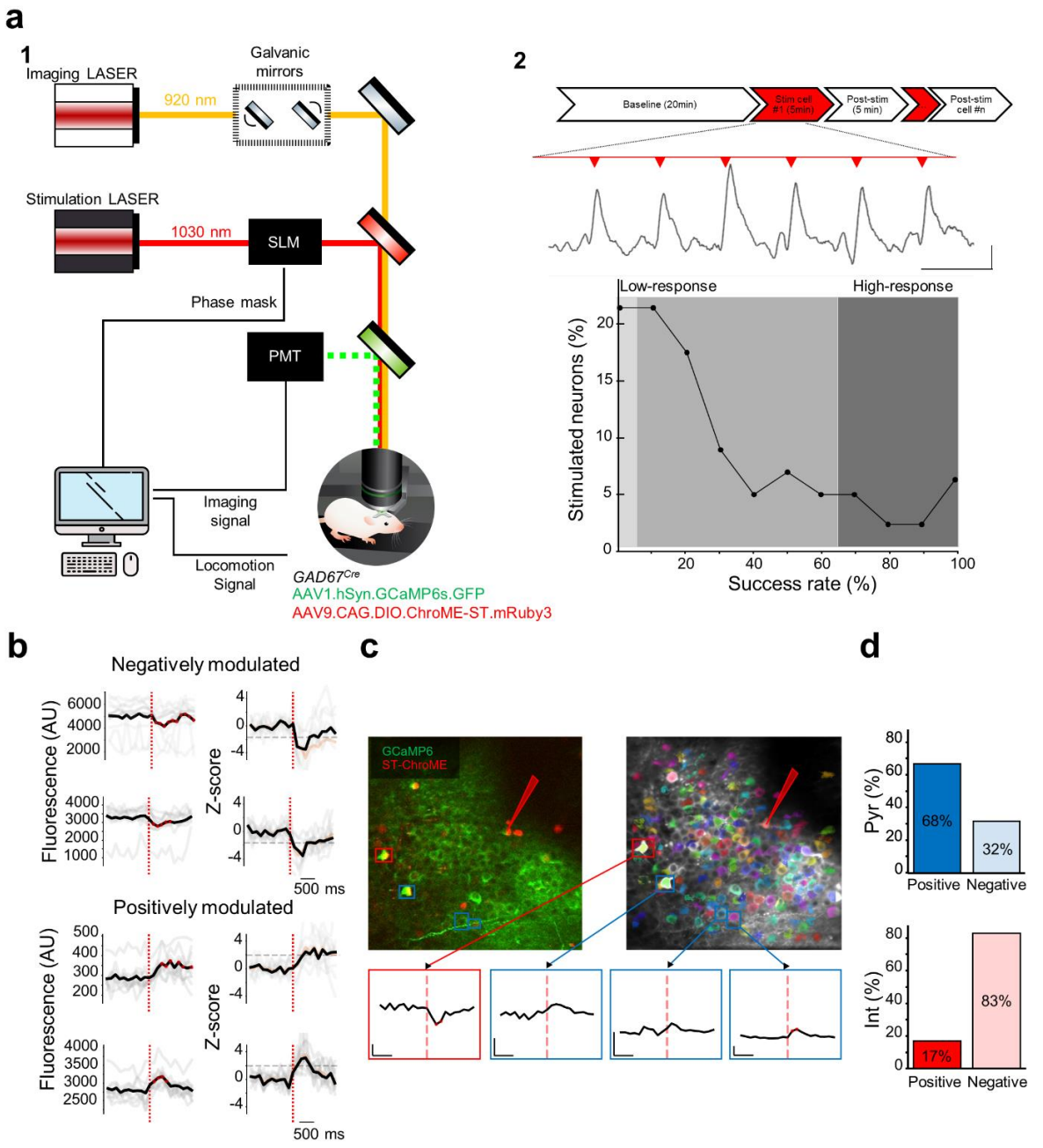

Figure 2 - Interneuron and pyramidal cell responses to single interneuron photoactivation.

a1. schematic representation of the custom-built optical set-up for targeted single-cell activation using holographic photostimulation combined with calcium imaging. Two LASER sources were employed for imaging and stimulation (920 and 1030 nm, respectively). The fast soma-targeted opsin ST-ChroME was co-expressed with GCaMP6m in GAD67-Cre mice. Mice were head-fixed and free to run on a self-paced treadmill. SLM: Spatial Light Modulator; PMT: PhotoMultiplier Tube. **a2.** Schematic of the experimental timeline with the fluorescence calcium trace of a stimulated interneuron (Stim cell) during the stimulation epoch. The graph represents the distribution of success rate (i.e. fraction of stimulation trials inducing a significant calcium fluorescence response) among the targeted interneurons co-expressing ST-Chrome and GCaMP6m (149 interneurons, 11 mice). **b**. Representative example fluorescence traces (left) of 4 imaged neurons negatively (top) or positively (bottom)

modulated by photoactivation of a single interneuron. The z-score (right) of their response was used to define significantly modulated neurons. The dashed red line indicates the time of stimulation). **c.** *Left,* representative field of view of the CA1 region imaged in a head-fixed mouse *in vivo.* GCaMP6m (green) is expressed in all neurons, whereas ST-Chrome (red) is present only in GABAergic neurons. The photo-stimulated cell is indicated by an arrow. *Bottom*, example stimulation-triggered fluorescence traces of non-stimulated interneurons (red) and pyramidal cells (blue). Right image indicates the segmented contour map of imaged neurons using Suite2P[84]. Scale bar: x: 500ms, y: 5% fluorescence signal. **d.** Bar plots of the distribution of positively (blue)- vs. negatively (red)- modulated neurons among the pyramidal cells (top) and interneurons (bottom).

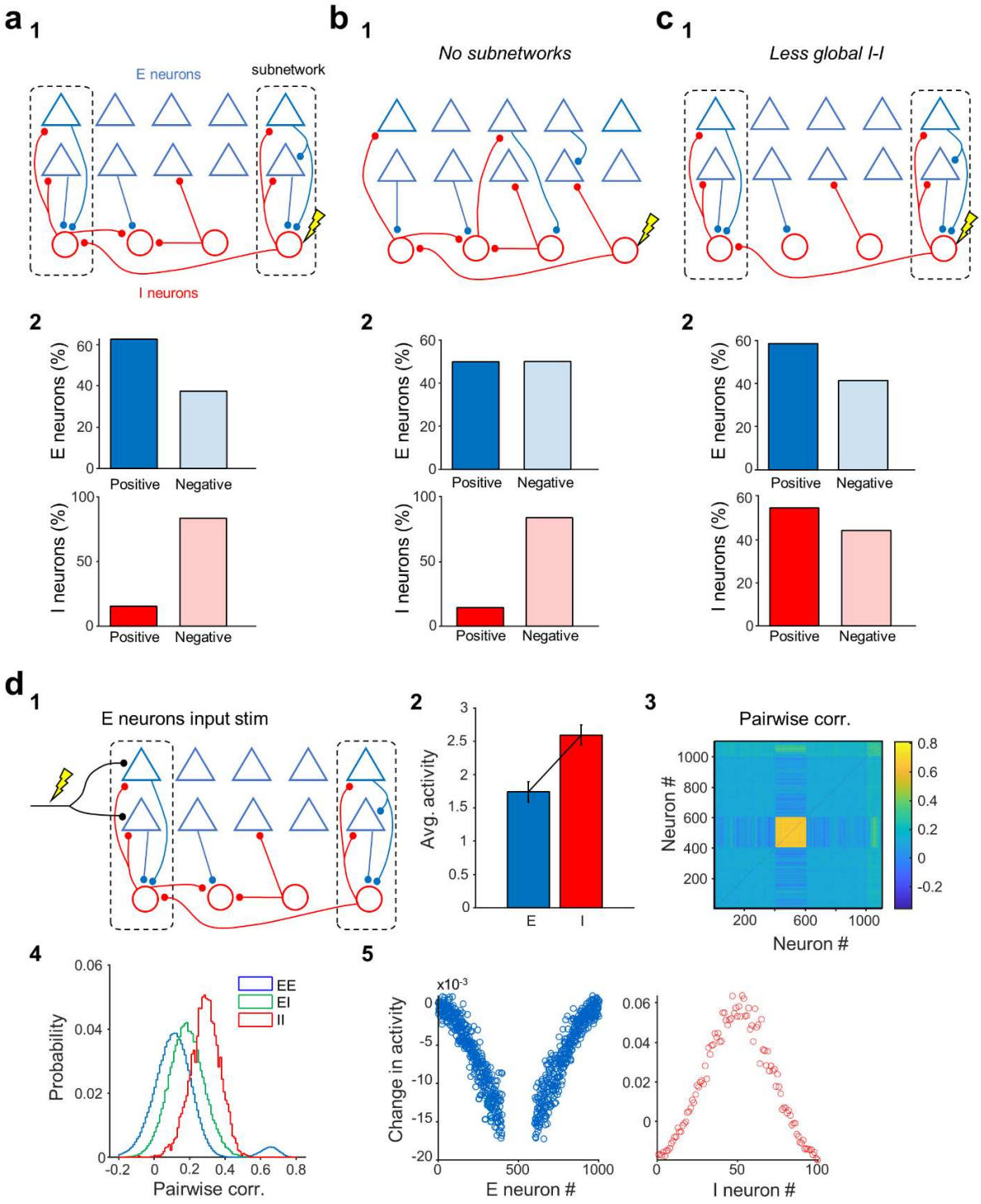

Figure 3 - Circuit mechanisms of the dichotomous effects of inhibition.
a1. Schematic depicting the structure of connectivity in the network model. Excitatory (E) and inhibitory (I) neurons are organized in subnetwork structure, whereby neurons belonging to similar subnetworks have higher weights of connectivity. This is implemented by a subnetwork weight modulation factor, which is most specific for E-E and E-I synapses (m_EE = m_EI = m_IE = 1) and nonspecific for I-I connections (m_II = 0). Connection probabilities are different for different connection types, with E-E connections being drawn very sparsely (1%), E-to-I and I-to-E connections more densely (50%), and I-I connections the densest (80%) (see Methods for details). **a2.** Fractions of E and I neurons showing a net positive (Pos) or negative (Neg) change in their activity, as a result of single I perturbations. All the I neurons in the

network are perturbed individually, and the average effect from all perturbations are plotted. **b1.** Same as a1, when the structure of the network connectivity lacks subnetworks (m_EE = 0, m_EI = 0, m_IE = 0, m_II = 0). **b2.** Fraction of positive and negative responses in the 'no subnetworks' condition (b1). **c1**. The structure of connectivity is the same as in (a1), but I-I connections have the same density (50%) and specificity as E-I connections (m_II = 1). **c2.** Fraction of positive and negative responses in the 'less global I-I' condition' (c1). **d1.** Same as a1, but with consistent stimulation of the excitatory inputs onto 20% of E neurons of the network (see Methods for details). **d2.** Average activity of E and I neurons in response to external stimulation depicted in d1. Error bars represent standard deviations. **d3-d4.** Pairwise correlations between E (#1-1000) and I (#1001-110) neurons in the network, following external stimulation. The distributions of correlations for different connection types (E-E, E-I and I-E) are shown on the right. **d5.** Changes in the activity of E (left) and I (right) neurons, as a result of stimulating a fraction of E neurons. The stimulated E neurons (in the middle) have a much higher increase in their activity as a result of direct stimulation and are hence not shown for illustration purposes. Neurons are organized according to their proximity in the subnetwork structure, namely closeby neurons have a higher weight of connections, if their connection type is specific.

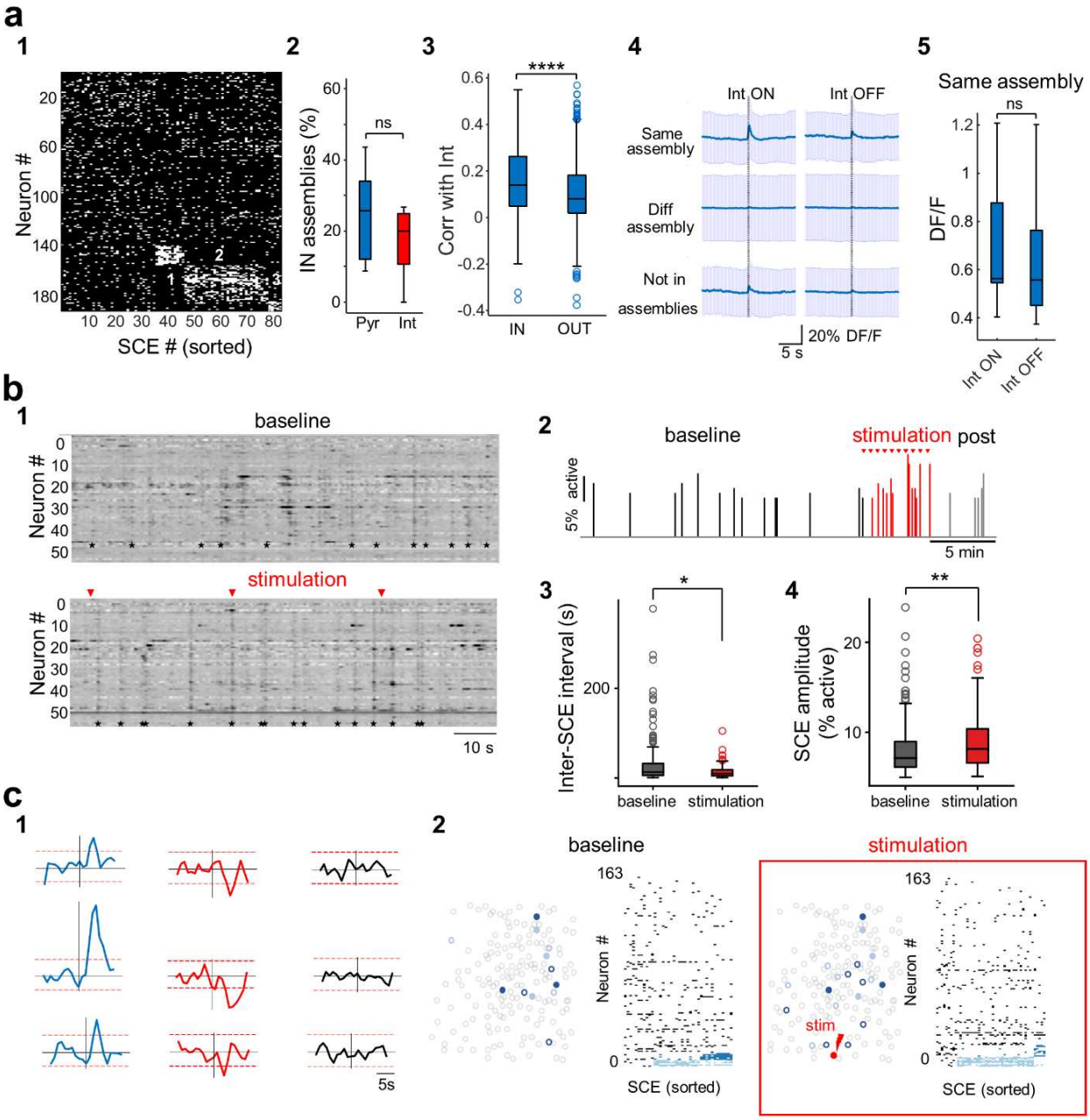

Figure 4 - Interneurons influence SCEs and pyramidal cell assemblies.

a1. Raster plot of all SCEs, within one representative imaging session, sorted by cell assemblies detected using the k-means SCE method (see Methods for details). The 3 significant cell assemblies are numbered. **a2.** Pyramidal cells and interneurons are recruited in cell assemblies in similar proportions (p=0.51, Wilcoxon signed-rank test, n=11 recordings from 6 mice). **a3**. Pyramidal cells that are part of cell assemblies show higher Pearson's correlations to interneurons compared to pyramidal cells not forming cell assemblies ($p=4e^{-11}$, Mann Whitney U test, pyramidal cells in assemblies: n=49; pyramidal cells not in assemblies: n=361, 11 recordings, 6 mice). **a4.** Lack of evidence of cell assembly segregation by single interneurons. Assembly activation-triggered average of pyramidal cells' calcium traces when each interneuron in an assembly is active (left) or inactive (right). Shaded areas represent standard deviations. *Top*, traces from pyramidal cells in the same assembly as the interneuron. *Middle*, traces from pyramidal cells in different assemblies. *Bottom*, traces from

pyramidal cells not forming assemblies. Note that the activity of the interneuron in an assembly does not affect the activity of pyramidal cells of competing assemblies or of the ones not forming assemblies. **a5.** No significant difference in ΔF/F peak at assembly activation for pyramidal cells when the interneuron in the same assembly is active or inactive ($p = 0.7$, Wilcoxon signed-rank test, $n = 7$ recordings with significant assemblies from 5 mice). Data from 21 cell assemblies. **b1.** Raster heatmaps of the relative changes in fluorescence as a function of time for all active imaged neurons in a representative example, during baseline (top) and stimulation (bottom). Stimulation time points are indicated by red triangles. Note the increase in SCE (black stars) occurrence during stimulation **b2.** Histogram of the fraction of active cells in each detected SCE as a function of time during the course of an entire experiment. Note the increase in SCE amplitude during stimulation (red) **b3.** Box plots comparing the inter-SCE intervals during baseline and stimulation periods ($p=0.01$, Mann Whitney U test) for “high-response” cells. **b4.** Box plots comparing SCE amplitude (fraction of active neurons) during baseline and stimulation periods ($p=0.007$, Mann Whitney U test) for “high response” cells. **c1.** Representative example traces of the median Z-score for members of the same assembly centered on the stimulation time. Assemblies are classified as activated (blue, left), suppressed (red, middle) or unmodulated (black, right) by the stimulation. Red dotted lines indicate significance thresholds (z-score>1,96 or <1,65, see methods) **c2.** Representative example showing the contour map and sorted SCE rasterplots for two assemblies (dark and light blue) detected during baseline (left) or stimulation and post-stim (right). Contours of neurons belonging to the same assembly during both epochs are filled.